

Full length article

The effect of orientation on the deformation behavior of Cr₂AlC

J.T. Pürstl^{a,*}, T.E.J. Edwards^{a,b}, F.D. León-Cázares^{a,c}, R.P. Thompson^a, N.M. della Ventura^d,
N.G. Jones^a, W.J. Clegg^a

^a Department of Materials Science and Metallurgy, University of Cambridge, 27 Charles Babbage Road, Cambridge CB3 0FS, United Kingdom

^b Laboratory for Mechanics of Materials and Nanostructures, EMPA, Swiss Federal Laboratories for Materials Science and Technology, Feuerwerkerstrasse 39, 3602 Thun, Switzerland

^c Sandia National Laboratories, 7011 East Avenue, Livermore, CA 94550, United States

^d Department of Materials, The University of California, Santa Barbara, CA 93106, United States

ARTICLE INFO

Keywords:

MAX Phases

Ceramics

Micromechanics

Non-Schmid

Dislocation Theory

ABSTRACT

The MAX phases are a group of ternary carbides and nitrides with potential for use in advanced high temperature applications. Numerous studies have shown their main deformation mechanism to be basal plane slip, even in extreme orientations, yet the fundamentals of this mechanism and dependencies on size and applied stress state remain inconclusive. Based on similar studies in Ti₃SiC₂, Ti₃AlC₂ and Ti₂AlC, the current work investigated the onset of basal plane slip as a function of loading orientation by compressing single crystal micropillars of Cr₂AlC. The results suggest clear changes in the critical resolved shear stress with loading orientation (non-Schmid effects), and attempts were made to rationalize this behavior by comparison with models of dislocation activity. On this basis, it is proposed that external influences on dislocation mobility are likely the governing factor in the observed non-Schmid effects in the MAX phases.

1. Introduction

The MAX phases, where M is a transition metal, A is an A group element and X is C or N, are a group of ternary carbides and nitrides with layered hexagonal crystal structures [1]. They are well known for their unusually high deformability that facilitates machinability and macroscopic deformation, whilst also retaining high hardness, high elastic moduli, and good high temperature stability. With this combination of properties, the MAX phases are widely regarded as attractive candidates for advanced high temperature applications, for example in the nuclear or aerospace industries [2–4].

Over the past two decades, numerous studies have focused on gaining a full picture of the mechanisms that give rise to the ductility of MAX phases [5–18]. Its origin was attributed mainly to the remarkably easy slip along the basal plane with critical resolved shear stresses (τ_{CRSS}) of as low as 77 MPa [5,16], coupled with the formation of kinks and similar structures that bend the crystal lattice [5–7,10,11,15,17–20]. Although other modes of plasticity have been reported under extreme stress states [8,21], the bulk of deformation is facilitated by basal plane shear and kink band formation, in both single crystals and

polycrystalline samples [5,6]. However, the exact mechanisms underlying basal plane slip are still widely debated.

Several transmission electron microscopy (TEM) and *ab initio* studies suggest basal plane dislocations with a Burgers vector $\frac{1}{3}a \langle 11\bar{2}0 \rangle$ to be the most likely dominant deformation mechanism [12,15,22]. Yet, in parallel, it has also been suggested that ripplocations, a completely different mechanism, are the element underlying basal plane slip, in a manner similar to other nanolayered structures such as mica [13]. This theory could substantiate the model of unstable, or incipient, kink band formation in MAX phases, which is believed by some authors to lie at the origin of the fully reversible hysteresis observed in cyclic loading of polycrystalline samples [6,13]. On this basis, ripplocations were also proposed to lie at the origin of a dependency of the τ_{CRSS} on the loading orientation, which was recently observed in micropillar compression of Ti₃AlC₂ and Ti₂AlC [17,18]. However, experimental as well as computational evidence for the existence of ripplocations is scarce, and both reversible hysteresis in MAX phases [11,23], and general changes of τ_{CRSS} with a change in loading axis [24–26], can also be explained by dislocation-based mechanisms.

A thorough understanding of MAX phase basal plane slip would not

* Corresponding author.

E-mail addresses: jpuerstl@uci.edu (J.T. Pürstl), thomas.edwards@empa.ch (T.E.J. Edwards), fleonca@sandia.gov (F.D. León-Cázares), rpt26@cam.ac.uk (R.P. Thompson), n.dellaventura@ucsb.edu (N.M. della Ventura), ngj22@cam.ac.uk (N.G. Jones), wjc1000@cam.ac.uk (W.J. Clegg).

<https://doi.org/10.1016/j.actamat.2023.119136>

Received 6 September 2022; Received in revised form 16 June 2023; Accepted 2 July 2023

Available online 17 July 2023

1359-6454/© 2023 The Authors. Published by Elsevier Ltd on behalf of Acta Materialia Inc. This is an open access article under the CC BY license (<http://creativecommons.org/licenses/by/4.0/>).

only be key to potentially facilitating the use of MAX phases in structural applications but may also provide a promising starting point for the development of similar toughened intermetallic-base materials for future high temperature applications [14].

As such, this work aimed to extend the current understanding of MAX phase deformation by basal plane slip through the compression of single crystal micropillars of Cr_2AlC . This approach allowed for basal plane slip to be targeted without the need to grow large single crystal samples, and facilitated direct comparison with other similar studies and models of basal plane slip. The primary aim was to further investigate the dependence of the critical resolved shear stress on the loading orientation, whilst tests of different pillar sizes were carried out to eliminate any effects of sample size [27]. On this basis, an approach is proposed by which the measured critical resolved shear stress for basal plane slip can be rationalized through dislocation mechanisms. The choice of material not only complements similar studies conducted in Ti_2AlC , Ti_3AlC_2 and Ti_3SiC_2 , but may also aid ongoing assessments of Cr_2AlC for industrial application [28–30].

2. Methods

A high purity polycrystalline bar of Cr_2AlC was produced at the Université de Poitiers through hot isostatic pressing (HIP) of elemental powders in stoichiometric quantities at 1450 °C and 50 MPa for 8 h. An outline of the processing procedure and the structural characterization of the thus produced compound can be found in reference [31]. A scanning electron micrograph (SEM) of the as-produced material, revealing dense Cr_2AlC grains with sizes ranging between 10 – 150 μm , is shown in Supplementary Figure S1. SEM analysis in combination with energy dispersive X-ray spectroscopy (EDS), also carried out at the Université de Poitiers, show small amounts of Al_2O_3 and Cr_3C_7 impurities accumulating along grain boundaries. A disk (~ 2 mm in height, 10 mm in diameter) was cut from the bar and parallel surfaces were achieved by grinding with SiC paper (800 – 2500 grit). One surface was subsequently polished using diamond suspensions (6 – 0.25 μm) and, in the final step, a buffered colloidal silica (OPS) solution (pH 7, 0.04 μm).

Electron backscatter diffraction (EBSD) was performed in a ZEISS GeminiSEM equipped with an Oxford Instruments Symmetry Detector, using an acceleration voltage of 20 kV and a tilt angle of 70°. Orientation

maps were generated using the AZtecHKL software (Oxford Instruments) at a step size of 2 μm . Indexing of the Kikuchi patterns was carried out based on the standard reference crystal parameters determined by Jeitschko et al. [32] ($a = 2.86$ Å, $c = 12.82$ Å), which are in accordance with the crystallographic parameters determined in reference [31]. Further orientational analysis, including Schmid factor calculation, was carried out using MTEX [33].

Cylindrical pillars for micro-compression testing were prepared using annular focused ion beam (FIB) milling in an FEI Helios Nanolab dual beam FIB/SEM, operated at 30 kV. Pillar preparation was carried out in single grains in multiple steps with decreasing ion beam current to optimize milling time whilst minimizing ion beam induced damage. Pillars were fabricated with nominal diameters of 1, 2, 3.5, 5 and 7 μm . The final milling step was carried out at 30 pA for the 1 μm pillar and 50 pA for all remaining pillar sizes, resulting in a reduction of the average pillar taper to below 3°. To optimize the pillar-punch alignment [34], all pillars were milled in the bulk of the chosen grains, so as to avoid any etch rounding near grain boundaries that might have arisen during sample preparation.

All pillars were compressed in situ using an Alemnis nanoindenter within a ZEISS CrossBeam FIB/SEM. A 5 μm diameter flat punch was used for compression of the 1 μm pillar, and a 10 μm diameter punch for compressing all of the other pillar sizes (both obtained from Synton MDP). Pillar compression was carried out in displacement control to a maximum strain of 5%, at constant displacement rate corresponding to an initial strain rate (normalized by pillar height) of 10^{-3} s^{-1} .

3. Results

An EBSD map of the as-produced material is shown in Fig. 1. From this information, several grains were selected for pillar milling to give a range of different crystal orientations, with Schmid factors for basal plane slip varying between 0.50 and 0.01. A summary of all pillar orientations is provided in Supplementary Table S1. Pillars of all sizes were prepared in high Schmid factor orientations ($\text{SF} > 0.47$) and a broad range was fabricated in low Schmid factor orientations; either with the basal plane almost parallel to the loading axis (e.g., Grain 11), or with the basal plane approaching 90° to the loading axis (e.g., Grains 8, 9, 10).

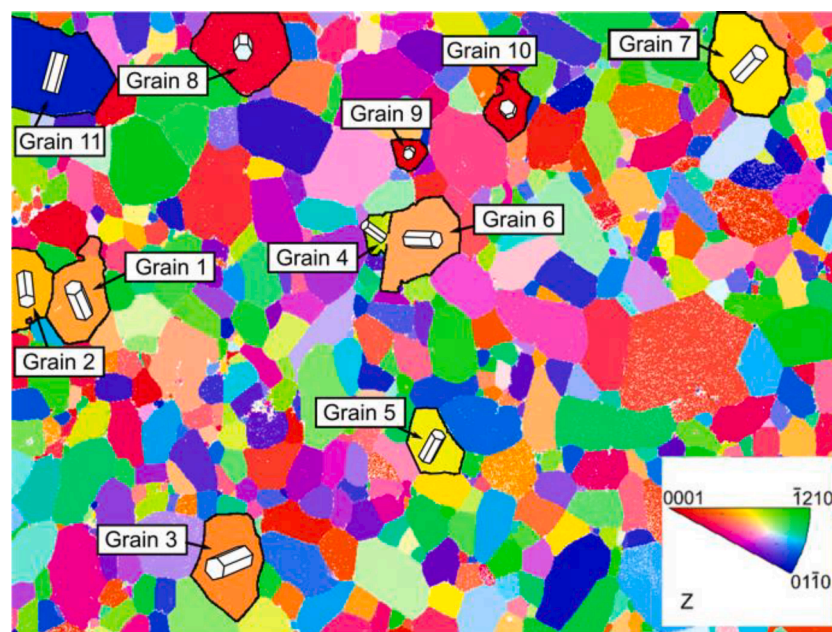


Fig. 1. EBSD map with grains selected for micropillar investigation. The color scheme refers to inverse pole figure (IPF) coloring, with the reference color scheme indicated in the inset. The selected grains and their crystal orientation are marked in the map.

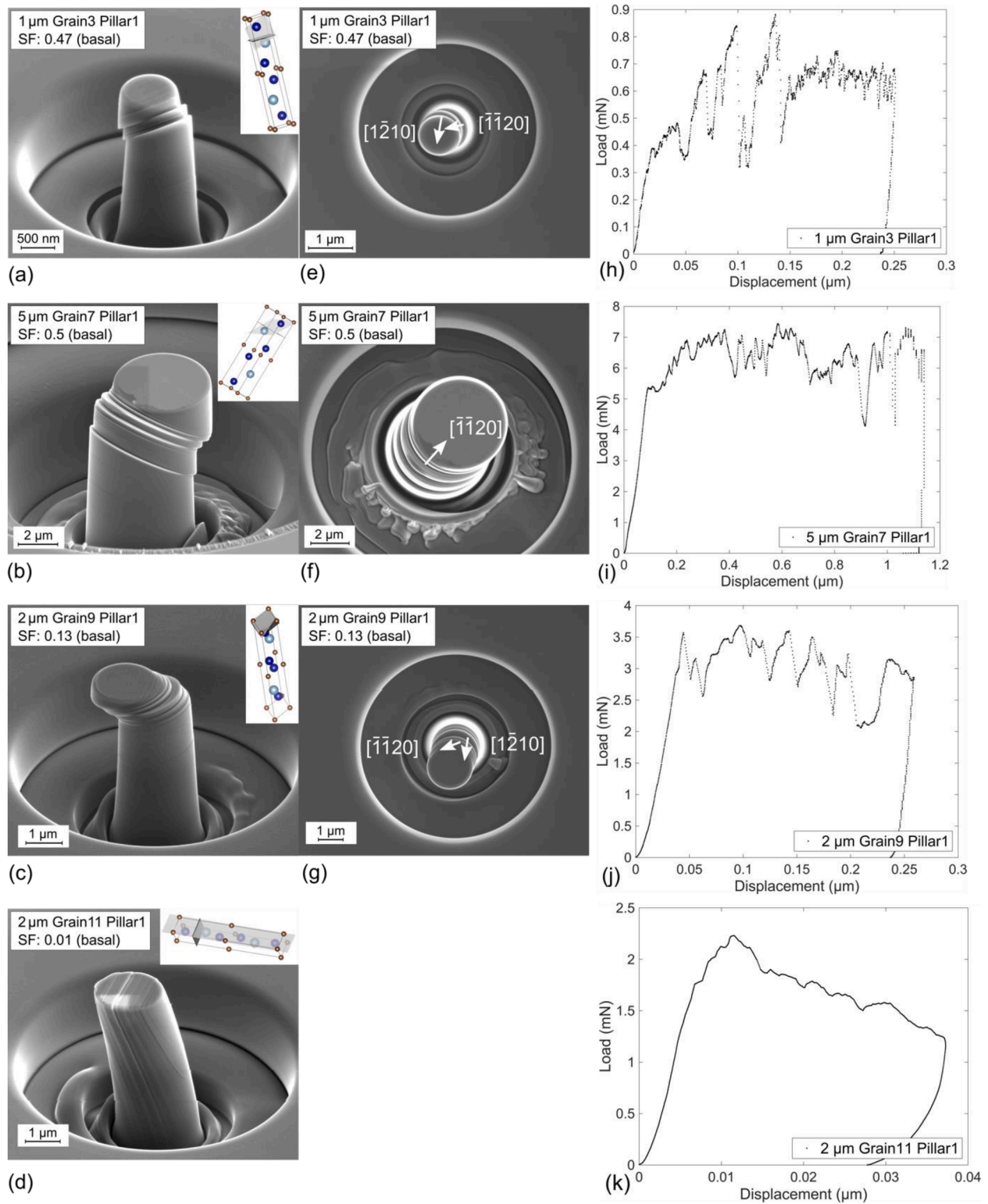


Fig. 2. Post compression images (a) – (d), slip directions activated (e) – (g) and load displacement curves (h) – (k) for pillars with varying orientation (representative selection). (a),(e),(h) 1 μm pillar in Area 3 (Schmid factor 0.47). Activated slip directions are $[\bar{1}\bar{1}20]$ (SF 0.47) and $[\bar{1}\bar{1}20]$ (SF 0.29). (b),(f),(i) 5 μm pillar in Area 7 (Schmid factor of 0.5). Activated slip directions are $[\bar{1}\bar{1}20]$ (SF 0.50). (c),(g),(j) 2 μm pillar in Area 9 (Schmid factor 0.13). Activated slip directions are $[\bar{1}\bar{1}20]$ (SF 0.13) and $[\bar{1}\bar{1}20]$ (SF 0.09). (d),(k) 2 μm pillar in Area 11 (Schmid factor 0.006); both, post compression image and loading curve suggest that the pillar bent during compression.

Table 1

Orientational information, σ_y and τ_{CRSS} for pillars shown in Fig. 2. Orientational reference is stated by means of the miller indices of loading axis, the angle φ between slip plane (0001) and loading axis, the angle λ between slip direction $\langle 11\bar{2}0 \rangle$ and loading axis (for maximum SF) and the Schmid factor $\cos\varphi\cos\lambda$.

	Crystallographic Loading Axis	φ (°)	λ (°)	Schmid factor for (0001) $\langle 11\bar{2}0 \rangle$	σ_y (MPa)	τ_{CRSS} (MPa)
1 μm						
Grain3 Pillar1	[−0.1488 −0.2455 0.3943 −0.1884]	35.27	55.13	0.47	964 ± 7	453 ± 3.3
2 μm						
Grain9 Pillar1	[−0.0170 −0.1378 0.1548 0.2236]	7.69	82.49	0.13	1210 ± 8	157 ± 1.04
Grain11 Pillar1	[0.0288 −0.6111 0.5823 0.0017]	89.57	27.61	0.01	–	–
5 μm						
Grain7 Pillar1	[−0.2389 −0.2524 0.4913 0.1619]	14.25	77.03	0.22	320 ± 22	160 ± 4.84

All compressed pillars deformed by basal plane slip, with exemplar images shown in Fig. 2a–d. It was noted that the slip directions linked to the highest Schmid factor were activated for most pillars as predicted, but deviations were observed for some pillars with a smaller diameter (1–2 μ m) or low Schmid factor orientations (SF < 0.22). In these cases, slip was observed to proceed along multiple slip directions. Examples of compressed pillars are shown in Fig. 2e–g. The related τ_{CRSS} were evaluated based on the highest Schmid factor orientations only.

Load displacement data for the compressed pillars shown in Fig. 2a–d are given in Fig. 2h–k. Yield stresses (σ_y) for the onset of basal plane slip were determined based on the method proposed in [35], where individual load drops were selected for yield stress determination. The primary indicator for selection was taken to be the displacements at which load drop events occur, which were then compared to slip steps formed in the pillar, in an attempt to create a pillar deformation history. In particular, this approach should allow for any marked changes in pillar cross section to be detected, for example where slip steps intersect the top of the pillar, or where slip steps proceed along multiple slip directions, such that subsequent stress calculations may be adjusted where necessary. Slip through the pillar top may be expected at the start of the loading cycle, as a consequence of initial alignment between punch and pillar. Particles or misalignment between pillar top and punch surfaces are likely causes of such deformation. Yield points were thus selected after initial low load regions in the plastic regime of the loading curves. The here stated σ_y are averages from all determined yield point-load drop combinations selected from a given pillar, as also proposed previously [35].

The average σ_y and the related τ_{CRSS} for the (0001) $\langle 11\bar{2}0 \rangle$ slip systems with the highest Schmid factor are summarized in Table 1 for the exemplary pillars stated. No values were considered for 2 μ m Grain 11 Pillar 1, given that severe bending (and thus induced reorientation of the basal plane) and the uncertainty of selecting a cross section for stress conversion [35] renders the confidence of any stress calculation too low for further analysis. Values for the remaining pillars are given in Supplementary Table S1.

4. Discussion

4.1. Basal plane slip

Within the present work, the sole operating deformation mechanism observed in all pillars was basal plane slip. No slip steps along any other slip system were observed, nor were any other deformation mechanisms, such as twinning, detected based on the morphologies of the deformed pillars. This substantiates previous research, e.g., in reference [8], which concluded that the shear stresses required for activation of slip on other slip systems, or twinning, are markedly higher compared to basal plane slip in the MAX phases. Such prevalence of basal plane deformation was also reported for micro-compression testing in the MAX phases Ti₂AlC [17], Ti₃SiC₂ [15], Ti₂InC and Ti₄AlN₃ [10], where this was accompanied by kinking, or fracture/delamination parallel to the basal plane. The absence of any such failure in the current study may be associated with the displacement-controlled indenter system employed (in

combination with small applied displacement rates), which avoids the large strain bursts often observed with load-controlled indenter systems, and hence excessive deformation and potentially catastrophic failure of the pillar. It is noted that, as the pillar sizes in the above-mentioned studies are comparable to those in the present study, size effects are unlikely to explain the observed inhibition of kinking, fracture or delamination.

4.2. Size effects

Plots of the critical resolved shear stresses necessary to activate basal plane slip as a function of pillar size are shown in Fig. 3a and reveal a distinct size effect in Cr₂AlC. In line with previous observations in numerous materials [27,36–46], the data in Fig. 3a may be described by a power law relationship, which is commonly stated as:

$$\tau_{CRSS} = Ad^{-m} \quad (1)$$

where A is a constant, m is the power law exponent and d is the pillar diameter.

Size effect data in Fig. 3a has been obtained from different pillar orientations. These can be roughly grouped into three classes by Schmid factor: high Schmid factor (SF > 0.47), medium Schmid factor (SF = 0.22) and low Schmid factor (SF = 0.13). Fig. 3b shows a fit of Eq. (1) to pillars with a high Schmid factor. This approach is consistent with the methodology most commonly used in the literature and enables comparison with early studies in fcc and bcc metals [27,43]. The power law exponent, $m = 0.65$, lies in the fcc metals range [41,43].

Further consideration of data in Fig. 3a reveals that the size effects appear to vary with varying Schmid factor; in particular, the data for pillars with medium Schmid factor (SF = 0.22) and low Schmid factor (SF = 0.13) orientations is consistently lower than for the high Schmid factor orientations (SF > 0.47). A quantitative reference of this effect is further shown in Fig. 3b, considering data from medium Schmid factor orientations, which gives a power law exponent $m = 0.48$. This indicates a change in the size dependence of the high and medium Schmid factor orientations. A similar observation was also made by Byer and Ramesh [47] for basal plane slip activated in micropillar compression of another hexagonal material, Mg, in comparable orientations.

A rationalization of the discrepancy in the size effects for different grain orientations was attempted by assessing the parameters likely to influence micropillar deformation behavior. For this purpose, the single-arm dislocation source model of Parthasarathy et al. [48] was employed, which is commonly used to explain the size-dependent strength of micropillars [43,46]. This model is limited to micropillars where deformation is facilitated by individual dislocation sources (source-controlled behavior).

Parthasarathy et al. [48] predicted that the resolved shear yield strength in micropillars can be estimated by

$$\tau_{CRSS,cal} = \tau_0 + \tau_T + \tau_{FR}(D) \quad (2)$$

where τ_0 denotes the friction stress (lattice resistance), τ_T is a forest (Taylor) hardening term and τ_{FR} is the stress needed to operate a half Frank-Read or single-arm dislocation source. Whilst τ_0 and τ_T are

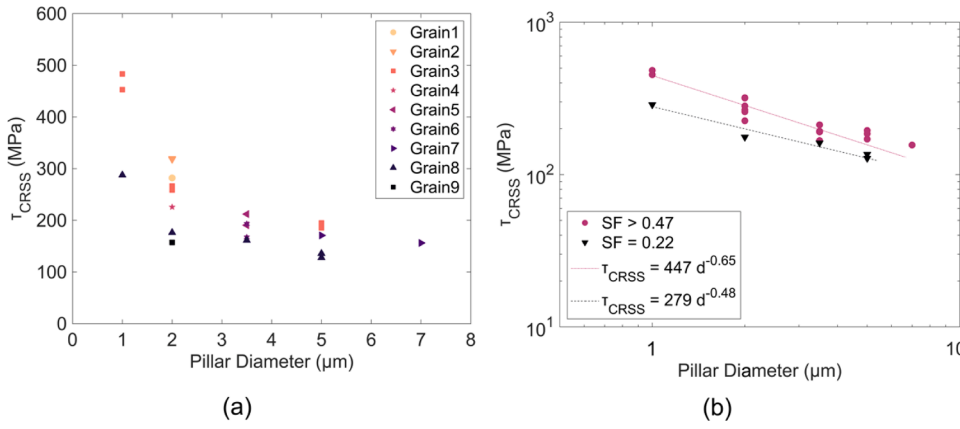


Fig. 3. Size effects as observed in the compressed Cr_2AlC micropillars. (a) τ_{CRSS} as a function of pillar diameter for all orientations tested. A decrease in τ_{CRSS} for low Schmid factor orientations can be observed. It is noted that all data with regards to a τ_{CRSS} was computed using the maximum basal plane Schmid factor for each orientation, which in the case of multiple slip direction activation would lead to a slight overestimate of the τ_{CRSS} values. (b) Power law fits related to the data for pillars with a high Schmid factor (SF > 0.47), to allow for a comparison with the literature, and for the medium Schmid factor orientations (Schmid factor = 0.22), to highlight the effect of a variation in size effect for varying pillar orientation.

nominally pillar-size independent, τ_{FR} is taken as a bowing stress and, thus, is a function of pillar dimensions,

$$\tau_{FR} = \frac{\alpha G b}{\bar{\lambda}_{\max}} \quad (2.1)$$

where α is a geometric factor, G is the shear modulus, b the Burgers vector of the dislocation, and $\bar{\lambda}_{\max}$ is the average arm length of the source. This latter value is generally taken to be the (on average) statistically longest, and thus weakest, source on a given slip plane in a pillar with a given diameter.

As suggested in [48], $\bar{\lambda}_{\max}$ can be evaluated via the probability of finding a source with length λ_{\max} in a (statistically valued) sample of slip planes with their normal lying at an angle φ from the loading axis and containing a sample of n randomly distributed pins within a pillar of diameter D (or radius R), a homogeneously distributed total dislocation density ρ_{tot} , height h and number of slip systems s , through:

$$\bar{\lambda}_{\max} = \int_0^R \left[1 - \frac{\pi(R - \lambda_{\max})(B - \lambda_{\max})}{\pi R B} \right]^{n-1} \times \left(\frac{\pi[(R - \lambda_{\max}) + (B - \lambda_{\max})]}{\pi R B} \right) n \lambda_{\max} d\lambda_{\max} \quad (2.2)$$

where $B = R/\cos\varphi$. The number of pins, n , is determined by the mobile dislocation density $\rho_{\text{mob}} = \frac{\rho_{\text{tot}}}{s}$ and the pillar dimensions, through $n = \frac{\rho_{\text{tot}} \pi R h}{s}$.

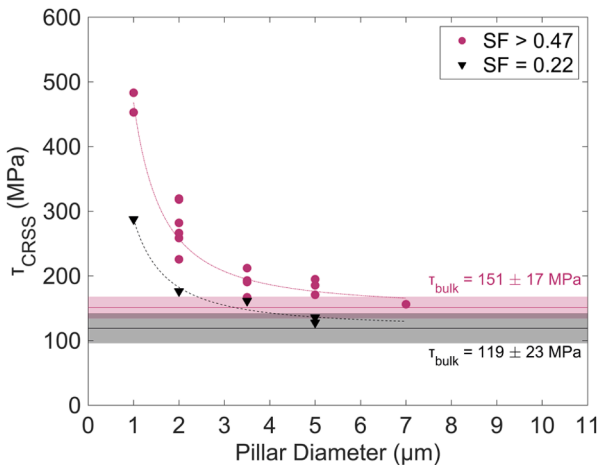


Fig. 4. Determination of asymptotic stress values for high and medium Schmid factor orientations, using a fitting function of the form $y = y_0 + qx^n$, where $y = y_0$ equals τ_{bulk} , to be used in Eq. (3). SF > 0.47: $q = 317$, $n = -1.58$; SF = 0.22: $q = 169$, $n = -1.42$.

Whilst the model does not predict an obvious dependency of either τ_0 or τ_T on parameters other than G or b , it does suggest that τ_{FR} is a function of pillar orientation ($\tau_{FR} = f(\varphi)$). To ascertain whether this functional relationship may partly rationalize the experimental trends observed in the current study, $\tau_{CRSS, \text{cal}}(D)$ (Eq. (2)) was computed for all tested orientations, assuming taper-free pillars with an aspect ratio of 2.75. $\tau_0 + \tau_T, \rho_{\text{tot}}$ as well as α were estimated for this purpose. An initial estimate of $\tau_0 + \tau_T$ was facilitated through comparison with the experimental results of the current study (Fig. 4), by taking

$$\tau_0 + \tau_T = \tau_{\text{bulk}} \quad (3)$$

based on the implied size-independence of these terms. The extraction of this value can indeed be promoted by questioning on the determination of the property volume element that governs the material and property description; that is, the existence of a length scale or dimension above which the value of stress remains constant. Small-scale testing performed at varying length scales can be used to delve into this aspect, empowering the extraction of the mentioned value. To this end, the values of τ_{bulk} were associated to the asymptotic value of the stress versus pillar diameter curve for each orientation. A specific fitting function was used for evaluation: $y = y_0 + qx^n$, with $y = y_0$ being τ_{bulk} . The fitted power law function reveals a change in τ_{bulk} , with $\tau_{\text{bulk, high}} = 151 \pm 17 \text{ MPa}$ predicted from the high Schmid factor orientations, and $\tau_{\text{bulk, medium}} = 119 \pm 23 \text{ MPa}$ for the medium Schmid factor pillars. Unfortunately, with synthesis routes being limited to hot isostatic pressing or similar techniques, restricting the production of bulk single-crystalline MAX phase samples, the availability of literature data for comparison with the estimated values is limited. ρ_{tot} was estimated to $2 \times 10^{12} \text{ m}^{-2}$, following the work of Lee and Nix [43]. This moderates between the low dislocation densities observed in pristine MAX phase samples [22,49–52] with the elevated dislocation densities observed in FIB milled pillars [38,40,42,45]. As the geometric factor α is not linked to a definite value [48], it is here used as a scaling factor to enable the best fit between the model and the experimental data. A summary of all material parameters used for computation is given in Supplementary Table S2.

The results of the above computation are summarized in Fig. 5. Fig. 5a and 5b show the fits of Eq. (2) using α as the fitting parameter. For a dislocation density of $2 \times 10^{12} \text{ m}^{-2}$ a value of $\alpha = 2.8$ is obtained as the best fit (Fig. 5b). However, none of the calculated fits can predict the change in trends between high and medium Schmid factor orientations observed experimentally. Shown in Fig. 5c is in particular the variation of τ_{FR} , as the only factor dependent on pillar orientation in Eq. (2); contrary to the experimentally observed trends, τ_{FR} increases marginally with decreasing Schmid factor, due to the dependence of λ_{\max} on the angle from the loading axis φ (Eq. (2.2)). The main factor determining the experimentally observed variation in size effects is thus the variation in τ_{bulk} . Additionally, it was found that the trends observed in Fig. 3b

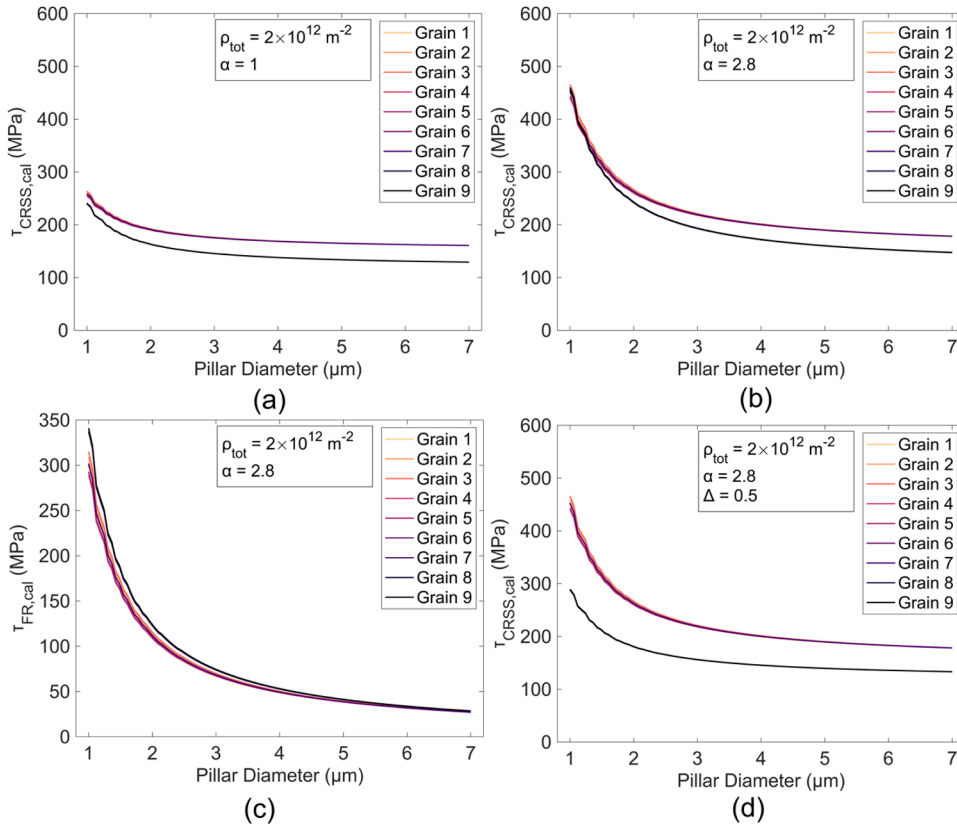


Fig. 5. Computational evaluation of micropillar compression size effects using the single-arm dislocation source model proposed by Parthasarathy et al. [48], Eq. (2). (a),(b) The geometric factor α was used as a fitting parameter. The closest fit to the experimental data, for $\rho_{\text{tot}} = 2 \times 10^{12} \text{ m}^{-2}$, was obtained for $\alpha = 2.8$. (c) Orientational dependence of the size dependent part of Eq. (2), $\tau_{\text{FR}} = \frac{\alpha G b}{\lambda_{\text{max}}}$. (d) The introduction of the parameter Δ in the size dependent term of Eq. (2), such that $\tau_{\text{FR,medium}} = \Delta \frac{\alpha G b}{\lambda_{\text{max}}}$, may explain the different power law relationships for the measured size effects for a Schmid factor < 0.22 (Grains 8 and 9) and a Schmid factor > 0.47 (Grains 1–7) (Fig. 3b).

could only be replicated if the term τ_{FR} for medium Schmid factor orientations were scaled by an additional factor Δ , such that $\tau_{\text{FR,medium}} = \Delta \frac{\alpha G b}{\lambda_{\text{max}}}$. A then obtained fit overlaps with the experimental data for $\Delta = 0.5$, as shown in Fig. 5d.

The need for this additional, non-physical factor Δ suggests that τ_{FR} varies with crystal orientation in a manner that cannot be accounted for by the orientational dependence of λ_{max} alone. If it is assumed that the single-arm dislocation source model suitably reflects the experimentally observed deformation of Cr_2AlC in the present study, then another parameter of $\tau_{\text{CRSS,cal}}$ (G , b , α , τ_0 or τ_1) must be a function of crystal orientation. Of the parameters of τ_{FR} it is most likely that α could be a parameter that changes with orientation. Nevertheless, as shown in Fig. 3b and implied in Eq. (3), τ_{bulk} varies with crystal orientation, so it is expected that one or both of τ_0 and τ_1 are dependent on orientation also. On this basis, it may be argued that the predicted scaling of τ_{FR} by Δ might additionally reflect a change in material parameters, potentially τ_0 .

4.3. Orientation effects

The evaluation of τ_{CRSS} from uniaxial testing is typically based on Schmid's law [53]. This is defined as $\tau_{\text{RSS}} = \sigma_a \cos \phi \cos \lambda$, where σ_a is the stress applied, $m_s = \cos \phi \cos \lambda$ is the Schmid factor, with ϕ as the angle between the loading direction and the slip plane normal and λ that between the loading and slip directions, and τ_{RSS} is the resolved shear stress. At the time of yield, this gives

$$\tau_{\text{CRSS}} = \sigma_y m_s, \quad (4)$$

from which the τ_{CRSS} for a particular slip system is commonly regarded a constant materials parameter. However, the data from the micropillar results obtained here show clear deviations from Schmid's law for the τ_{CRSS} for basal plane slip in Cr_2AlC . These are summarized as a function of the Schmid factor in Fig. 6. As such, a change in τ_{CRSS} with varying

orientation is an observation that is not expected from classical uniaxial mechanics, and hence is commonly referred to as non-Schmid behavior [24,25,54,55]. Such non-Schmid behaviors may be rationalized considering the effects of stress components other than the resolved shear stress on slip. Two examples are the stress normal to the slip plane (normal stress, σ_n) and the shear stress acting on the plane perpendicular to the Burgers vector (Escaig stress, τ_E).

Non-Schmid τ_{CRSS} effects have recently been reported also for micropillar compression of the MAX phases Ti_2AlC [17] and Ti_3AlC_2 [18]. The authors principally associated these findings with a change in the (compressive) stress normal to the slip plane, termed normal stress,

$$\sigma_n = \sigma_y \cos^2 \phi. \quad (5)$$

Zhan et al. [17,18] found that for both, Ti_2AlC and Ti_3AlC_2 , the τ_{CRSS}

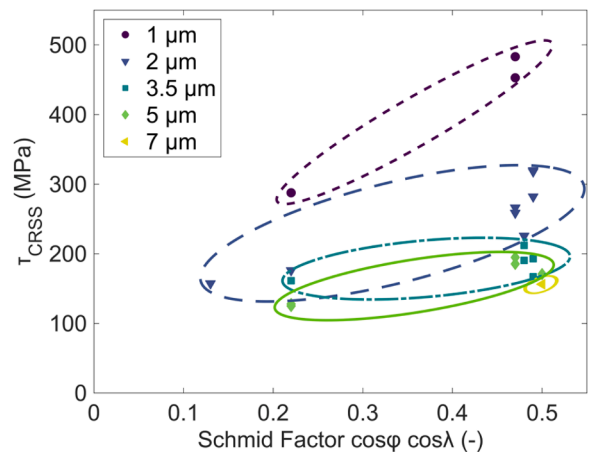


Fig. 6. Variation of τ_{CRSS} with a change in Schmid factor for micropillar compression of Cr_2AlC .

increased concomitantly with σ_n , and a functional relationship of the form $\tau_{CRSS} = \tau_0 + k\sigma_n$ was proposed. Here, τ_0 refers to the intrinsic critical resolved shear stress for basal plane slip (i.e., the critical resolved shear stress for pure shear, independent of a normal stress), and k is termed a frictional coefficient. The authors did not expound a mechanism behind the observed relationship, but a link was proposed between the present relationship and earlier results obtained from cyclic loading of MAX phases [6,13].

Normal stresses have been deemed responsible for non-Schmid effects also in several metals [54,56,57], where they are thought to originate from variations in the Peierls stress produced by a change in interatomic spacings [58].

The relationship between the τ_{CRSS} and the σ_n for the present study is shown in Fig. 7a for pillars with diameters of 1, 2, 3.5 and 5 μm . However, with the τ_{CRSS} seemingly decreasing for increasing values of σ_n , the trends observed by Zhan et al. [17,18] do not hold in the present study.

Several TEM studies [9,15,22] have confirmed the presence of basal plane dislocations in MAX phases. A dissociation of these dislocations into Shockley partials on the basal plane, bounded by an intrinsic stacking fault (ISF):

$$\frac{1}{3} a \langle 11\bar{2}0 \rangle \rightarrow \frac{1}{3} a \langle 10\bar{1}0 \rangle + \text{ISF} + \frac{1}{3} a \langle 01\bar{1}0 \rangle \quad (6)$$

has been shown recently by both, energy considerations obtained by *ab initio* studies [12,15], and HAADF-STEM [15].

By that means, another stress component that may have an influence on the observed effects is the Escaig stress [59]. This is the shear stress component that acts on the slip plane but perpendicular to the Burgers vector, which at the time of yield is calculated as

$$\tau_E = \sigma_y \cos \phi \cos \lambda_n, \quad (7)$$

where λ_n is the angle between the direction within the slip plane and normal to the Burgers vector, and the loading axis. While the Escaig stress has no effect on a perfect dislocation, it exerts Peach-Koehler type forces of equal magnitude but opposite directions on the individual partials [60]. In particular, this may affect the width of the extended stacking fault between partials, which has been argued to influence the mobility of the dislocation [59]. Positive Escaig stresses are hereby defined as those that promote an increase in the stacking fault width. In hcp crystals, half of the basal planes experience positive Escaig stresses while the other half experience negative ones for any non-zero Escaig stress [61]. The magnitude of the Escaig stresses are reported in the following analysis.

A complete partial decorrelation in Cr_2AlC is unlikely due to the high stacking fault energy (may be estimated to 0.5 - 1 J from calculations in Ti_2AlC [12] and Ti_3SiC_2 [15]), yet small variations may be possible. The relationship between the τ_{CRSS} and the τ_E for the present study is shown in Fig. 7b. A decreasing τ_{CRSS} with increasing τ_E is apparent, similar to the effect of σ_n .

The observed effects of σ_n and τ_E on τ_{CRSS} may be explained from a perspective of dislocation motion. Where a dissociation into partials is likely, both, an increasing σ_n and τ_E can result in an increase in the spacing between partials [60]; a widened dislocation core is obtained, decreasing the Peierls stress [62,63].

Nevertheless, from studies of non-Schmid effects in L_{12} ordered structures and bcc metals, non-Schmid effects may also arise from the structure of the dislocation cores [24,26]. It is noted that Peierls analysis assumes a planar dislocation core. However, recent studies by Plummer et al. [64] via molecular dynamics in Ti_3AlC_2 suggest a more complex

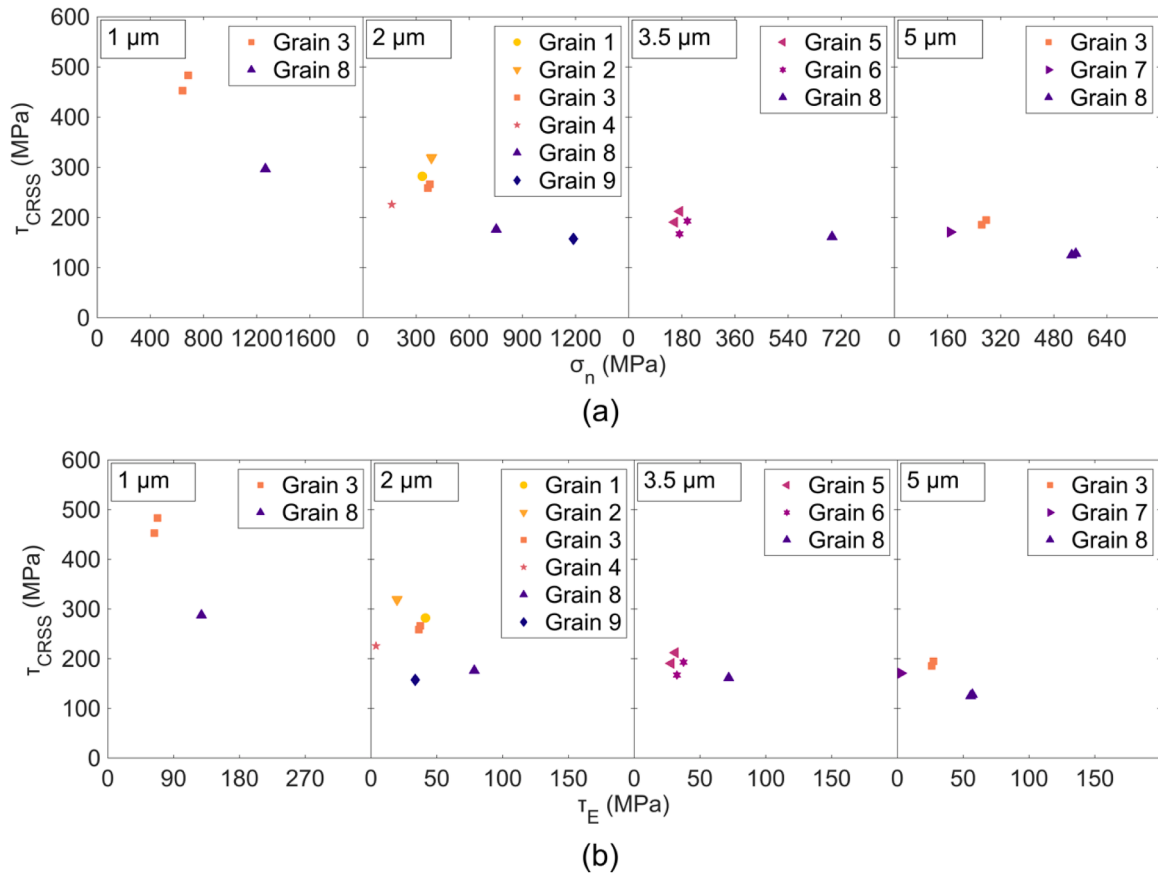


Fig. 7. Relationships between pillar strength (τ_{CRSS}) per size on stress components other than the resolved shear stress. (a) τ_{CRSS} as a function of the stress normal to the slip plane, σ_n . (b) τ_{CRSS} as a function of the Escaig stress, i.e., the shear stress within the slip plane normal to the Burgers vector, τ_E .

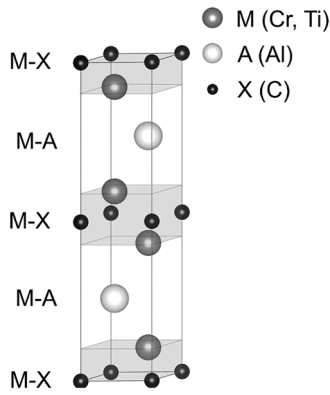


Fig. 8. MAX Phase unit cell with stoichiometry M_2AX , divided into M-A and M-X regions parallel to the basal plane. Basal plane dislocations glide between M and A (in the M-A layer), but are bounded by the (stronger) M-X layers.

dislocation structure in the MAX phases – in particular with dislocation pairs having been predicted as the stable dislocation configuration. While edge basal dislocation pairs appear planar, screw basal dislocation pairs partially extend onto the pyramidal planes, likely reducing their mobility. In bcc transition metals [26], or $L1_2$ alloys [24] non-planar screw dislocation cores may rearrange with an increase in τ_E , resulting in a more planar configuration. As no changes in core structures have been observed for σ_n up until 3 GPa in the MAX phases [64], the screw dislocation core may be equally altered by the influence of τ_E .

Importantly, any of the above effects do not mutually exclude the discrepancies observed between Ti_2AlC/Ti_3AlC_2 and Cr_2AlC . Basal plane slip in the MAX phases proceeds between the M and A layers [12,15]: the extent of a non-planar dislocation core into the pyramidal planes is thus bounded by the CrC and TiC layer respectively (Fig. 8). The Ti-Al and Cr-Al layers show differences in bonding [65,66], hence the extent of any non-planar dislocation component onto the pyramidal plane may differ between compositions for a given basal plane inclination with respect to the loading axis. In Ti_2AlC/Ti_3AlC_2 , this extent may be pronounced, resulting in decreased dislocation mobility on the basal plane (increased τ_{CRSS}) as the basal plane normal rotates towards the loading axis (which geometrically corresponds to increasing σ_n); in Cr_2AlC it may be however less pronounced, making other effects more dominant, such as an increased partial separation. Indeed, an additional compositional variation resides in the different stacking fault energy (which determines partial separation), and its dependency on externally applied pressure, for Cr-Al versus Ti-Al. A large increase in partial separation may be possible in Cr_2AlC , whereby it may be limited in Ti_3AlC_2/Ti_2AlC . Confirmation of the above effects remain matter of future investigations, as further *ab initio* analysis is required in all studied compositions.

Unfortunately, it is geometrically impossible to fully decouple the effects of the normal and Escaig stresses within uniaxial testing. Considering all possible stress states for uniaxial compression as predicted by the Mohr's circle, and recalling that the resolved shear and Escaig stress are the orthogonal components of the shear stress τ on the slip plane ($\tau^2 = \tau_{CRSS}^2 + \tau_E^2$) [67], the following expression is readily obtained:

$$\tau_{CRSS}^2 + \tau_E^2 = \sigma_n (\sigma_y - \sigma_n). \quad (8)$$

The coupling between different stress components, in particular σ_n and τ_{CRSS} , has already been noted by Barendregt and Sharpe [54], who instead tested under biaxial load to superimpose normal stresses for evaluation of non-Schmid effects in Zn. Consequently, to fully understand the nature of MAX phase deformation, we propose that further experimental investigation of the observed non-Schmid behavior must be able to establish effects of the normal and Escaig stresses independently, for example through the use of a pure shear setup.

5. Summary and Conclusions

Basal plane slip is widely observed to lie at the origin of the significant deformability of MAX phases, yet aspects of its operating mechanism remain inconclusive. The current work aimed to enhance our understanding of the dependence of τ_{CRSS} with loading orientation through single crystal micropillar compression of a Cr_2AlC MAX phase. The main findings were:

- Basal plane slip was observed as the only deformation mechanism regardless of pillar size and crystal orientation.
- The measured τ_{CRSS} showed an orientational dependence suggesting non-Schmid behavior, in line with recent observations in the Ti_3AlC_2 and Ti_2AlC MAX phases.
- A distinct size effect was measured, but this also appeared to be a function of orientation, which again implies non-Schmid behavior.
- However, the current results do not show the same relationship between τ_{CRSS} and the normal stress across the slip plane (σ_n) that has been previously used to rationalize non-Schmid behavior in Ti_2AlC and Ti_3AlC_2 .
- Alternatively, we propose a combination of normal stresses (stress normal to the slip plane) and Escaig stresses (stress perpendicular to the slip direction), versus a possible extension of dislocation cores onto pyramidal planes as a function of local compositional variation in the MAX phases, as possible origin of the observed behavior. In particular, we suggest that these factors influence the mobility of basal plane dislocations and the partials they dissociate into, through variation in dislocation core structure and changes in the extended stacking faults between partials.
- The results prompt further investigation by means of atomistic studies of different MAX phase compositions under varying stress states. Additional experimental investigation of these effects will require different methodologies, such as pure shear testing, to enable the influence of the normal and Escaig stresses to be resolved independently.

Declaration of Competing Interest

The authors declare that they have no known competing financial interests or personal relationships that could have appeared to influence the work reported in this paper.

Acknowledgements

The authors would like to thank Patrick Chartier and Thierry Cabioch at the Université de Poitiers for provision of the samples and their valuable advice on sample preparation. They would also like to thank Simon Griggs, Giorgio Divitini and John Walmsley for help with the SEM/FIB systems. Furthermore, their thanks go to Eric Tapley and Richard Langford for support with the small-scale testing equipment. Thanks also go to Professor Sandra Korte-Kerzel, Professor Ralph Spolenak and Professor Erik Bitzek for insightful discussions.

Colourscales used were taken from [68].

This project has received funding from the Euratom research and training program 2014–2018 under grant agreement No. 740415. T.E.J. E. received funding from EMPAPOSTDOCS-II of the European Union's Horizon 2020 research and innovation program under the Marie Skłodowska-Curie grant agreement number 754364.

Supplementary materials

Supplementary material associated with this article can be found, in the online version, at doi:10.1016/j.actamat.2023.119136.

References

- [1] M.W. Barsoum, The $M_{N+1}AX_N$ phases: A new class of solids: Thermodynamically stable nanolaminates, *Progress in solid state chemistry* 28 (1-4) (2000) 201–281.
- [2] T. Yang, C. Wang, C.A. Taylor, X. Huang, Q. Huang, F. Li, L. Shen, X. Zhou, J. Xue, S. Yan, Y. Wang, The structural transitions of Ti_3AlC_2 induced by ion irradiation, *Acta materialia* 65 (2014) 351–359.
- [3] D.J. Tallman, E.N. Hoffman, N.C. El'ad, B.L. Garcia-Diaz, G. Kohse, R.L. Sindelar, M.W. Barsoum, Effect of neutron irradiation on select MAX phases, *Acta Materialia* 85 (2015) 132–143.
- [4] J. Gonzalez-Julian, Processing of MAX phases: From synthesis to applications, *Journal of the American Ceramic Society* 104 (2) (2021) 659–690.
- [5] M.W. Barsoum, T. El-Raghy, Room-temperature ductile carbides, *Metallurgical and Materials Transactions A* 30 (2) (1999) 363–369.
- [6] M.W. Barsoum, T. Zhen, S.R. Kalidindi, M. Radovic, A. Murugiah, Fully reversible, dislocation-based compressive deformation of Ti_3SiC_2 to 1 GPa, *Nature Materials* 2 (2) (2003) 107–111.
- [7] A.G. Zhou, M.W. Barsoum, Kinking nonlinear elastic deformation of Ti_3AlC_2 , Ti_2AlC , $Ti_3Al(C_{0.5}N_{0.5})_2$ and $Ti_2Al(C_{0.5}N_{0.5})$, *Journal of alloys and compounds* 498 (1) (2010) 62–70.
- [8] C. Tromas, P. Villechaise, V. Gauthier-Brunet, S. Dubois, Slip line analysis around nanoindentation imprints in Ti_3SnC_2 : a new insight into plasticity of MAX-phase materials, *Philosophical Magazine* 91 (2011) 1265–1275.
- [9] A. Guitton, A. Joulain, L. Thilly, C. Tromas, Dislocation analysis of Ti_2AlN deformed at room temperature under confining pressure, *Philosophical Magazine* 92 (36) (2012) 4536–4546.
- [10] C. Brüsewitz, I. Knorr, H. Hofäss, M.W. Barsoum, C.A. Volkert, Single crystal pillar microcompression tests of the MAX phases Ti_2InC and Ti_4AlN_3 , *Scripta Materialia* 69 (4) (2013) 303–306.
- [11] N.G. Jones, C. Humphrey, L.D. Connor, O. Wilhelmsson, L. Hultman, H.J. Stone, F. Giuliani, W.J. Clegg, On the relevance of kinking to reversible hysteresis in MAX phases, *Acta materialia* 69 (2014) 149–161.
- [12] K. Gouriet, P. Carrez, P. Cordier, A. Guitton, A. Joulain, L. Thilly, C. Tromas, Dislocation modelling in Ti_2AlN MAX phase based on the Peierls–Nabarro model, *Philosophical Magazine* 95 (23) (2015) 2539–2552.
- [13] J. Gruber, A.C. Lang, J. Griggs, M.L. Taheri, G.J. Tucker, M.W. Barsoum, Evidence for bulk ripplications in layered solids, *Scientific reports* 6 (1) (2016) 1–8.
- [14] P.R. Howie, R.P. Thompson, S. Korte-Kerzel, W.J. Clegg, Softening non-metallic crystals by inhomogeneous elasticity, *Scientific reports* 7 (1) (2017) 1–9.
- [15] M. Higashi, S. Momono, K. Kishida, N.L. Okamoto, H. Inui, Anisotropic plastic deformation of single crystals of the MAX phase compound Ti_3SiC_2 investigated by micropillar compression, *Acta Materialia* 161 (2018) 161–170.
- [16] R.P. Thompson, W.J. Clegg, Predicting whether a material is ductile or brittle, *Current Opinion in Solid State and Materials Science* 22 (3) (2018) 100–108.
- [17] Z. Zhan, Y. Chen, M. Radovic, A. Srivastava, Non-classical crystallographic slip in a ternary carbide – Ti_2AlC , *Materials Research Letters* 8 (2020) 275–281.
- [18] Z. Zhan, Y. Chen, M. Radovic, A. Srivastava, On the non-classical crystallographic slip in $Ti_{n+1}AlC_n$ MAX phases, *Scripta Materialia* 194 (2021), 113698.
- [19] E. Orowan, A type of plastic deformation new in metals, *Nature* 149 (3788) (1942) 643–644.
- [20] F.C. Frank, A.N. Stroth, On the theory of kinking, *Proceedings of the Physical Society. Section B* 65 (10) (1952) 811.
- [21] C. Tromas, S. Parent, W. Sylvain, L. Thilly, G. Renou, C. Zehnder, S. Schröders, S. Korte-Kerzel, A. Joulain, Nanoindentation-induced deformation twinning in MAX phase Ti_2AlN , *Acta Materialia* 227 (2022), 117665.
- [22] L. Farber, M.W. Barsoum, A. Zavaliangos, T. El-Raghy, I. Levin, Dislocations and stacking faults in Ti_3SiC_2 , *Journal of the American Ceramic Society* 81 (6) (1998) 1677–1681.
- [23] A. Guitton, S. Van Petegem, C. Tromas, A. Joulain, H. Van Swygenhoven, L. Thilly, Effect of microstructure anisotropy on the deformation of MAX polycrystals studied by in-situ compression combined with neutron diffraction, *Applied Physics Letters* 104 (24) (2014), 241910.
- [24] S.S. Ezz, D.P. Pope, V. Paidar, The tension/compression flow stress asymmetry in Ni_3 (Al, Nb) single crystals, *Acta Metallurgica* 30 (5) (1982) 921–926.
- [25] J.W. Christian, Some surprising features of the plastic deformation of body-centered cubic metals and alloys, *Metallurgical transactions A* 14 (7) (1983) 1237–1256.
- [26] M.A.S. Duesbery, V. Vitek, Plastic anisotropy in bcc transition metals, *Acta Materialia* 46 (5) (1998) 1481–1492.
- [27] M.D. Uchic, D.M. Dimiduk, J.N. Florando, W.D. Nix, Sample dimensions influence strength and crystal plasticity, *Science* 305 (5686) (2004) 986–989.
- [28] Z.J. Lin, M.S. Li, J.Y. Wang, Y.C. Zhou, High-temperature oxidation and hot corrosion of Cr_2AlC , *Acta Materialia* 55 (18) (2007) 6182–6191.
- [29] Q. Huang, H. Han, R. Liu, G. Lei, L. Yan, J. Zhou, Saturation of ion irradiation effects in MAX phase Cr_2AlC , *Acta Materialia* 110 (2016) 1–7.
- [30] J.L. Smialek, J.A. Nesbitt, T.P. Gabb, A. Garg, R.A. Miller, Hot corrosion and low cycle fatigue of a Cr_2AlC -coated superalloy, *Materials Science and Engineering: A* 711 (2018) 119–129.
- [31] M. Jaouen, P. Chartier, T. Cabioch, V. Mauchamp, G. André, M. Viret, Invar Like Behavior of the Cr_2AlC MAX Phase at Low Temperature, *Journal of the American Ceramic Society* 96 (2013) 3872–3876.
- [32] W. Jeitschko, H. Nowotny, F. Benesovsky, Kohlenstoffhaltige ternäre Verbindungen (H-Phase), *Monatshefte für Chemie und verwandte Teile anderer Wissenschaften* 94 (1963) 672–676.
- [33] F. Bachmann, R. Hielscher, H. Schaeßen, Grain detection from 2d and 3d EBSD data—Specification of the MTEX algorithm, *Ultramicroscopy* 111 (12) (2011) 1720–1733.
- [34] R. Soler, J.M. Molina-Aldareguia, J. Segurado, J. Llorca, Effect of misorientation on the compression of highly anisotropic single-crystal micropillars, *Advanced engineering materials* 14 (11) (2012) 1004–1008.
- [35] J.T. Pürstl, H.O. Jones, T.E.J. Edwards, R.P. Thompson, F. Di Gioacchino, N. G. Jones, W.J. Clegg, On the extraction of yield stresses from micro-compression experiments, *Materials Science and Engineering: A* 800 (2021), 140323.
- [36] C.A. Volkert, E.T. Lilleodden, Size effects in the deformation of sub-micron Au columns, *Philosophical Magazine* 86 (33-35) (2006) 5567–5579.
- [37] C.P. Frick, B.G. Clark, S. Orso, A.S. Schneider, E. Arzt, Size effect on strength and strain hardening of small-scale [1 1 1] nickel compression pillars, *Materials Science and Engineering: A* 489 (1-2) (2008) 319–329.
- [38] S.I. Rao, D.M. Dimiduk, T.A. Parthasarathy, M.D. Uchic, M. Tang, C. Woodward, Athermal mechanisms of size-dependent crystal flow gleaned from three-dimensional discrete dislocation simulations, *Acta Materialia* 56 (13) (2008) 3245–3259.
- [39] A.S. Schneider, D. Kaufmann, B.G. Clark, C.P. Frick, P.A. Gruber, R. Mönig, O. Kraft, E. Arzt, Correlation between critical temperature and strength of small-scale bcc pillars, *Physical review letters* 103 (10) (2009), 105501.
- [40] A.T. Jennings, M.J. Burek, J.R. Greer, Microstructure versus size: mechanical properties of electroplated single crystalline Cu nanopillars, *Physical review letters* 104 (13) (2010), 135503.
- [41] S. Korte, W.J. Clegg, Discussion of the dependence of the effect of size on the yield stress in hard materials studied by microcompression of MgO, *Philosophical Magazine* 91 (7-9) (2011) 1150–1162.
- [42] R. Gu, A.H.W. Ngan, Effects of pre-straining and coating on plastic deformation of aluminum micropillars, *Acta materialia* 60 (17) (2012) 6102–6111.
- [43] S.W. Lee, W.D. Nix, Size dependence of the yield strength of fcc and bcc metallic micropillars with diameters of a few micrometers, *Philosophical Magazine* 92 (10) (2012) 1238–1260.
- [44] A.S. Schneider, C.P. Frick, E. Arzt, W.J. Clegg, S. Korte, Influence of test temperature on the size effect in molybdenum small-scale compression pillars, *Philosophical Magazine Letters* 93 (6) (2013) 331–338.
- [45] R. Soler, J.M. Wheeler, H.J. Chang, J. Segurado, J. Michler, J. Llorca, J.M. Molina-Aldareguia, Understanding size effects on the strength of single crystals through high-temperature micropillar compression, *Acta materialia* 81 (2014) 50–57.
- [46] O.T. Abad, J.M. Wheeler, J. Michler, A.S. Schneider, E. Arzt, Temperature-dependent size effects on the strength of Ta and W micropillars, *Acta Materialia* 103 (2016) 483–494.
- [47] C.M. Byer, K.T. Ramesh, Effects of the initial dislocation density on size effects in single-crystal magnesium, *Acta materialia* 61 (10) (2013) 3808–3818.
- [48] T.A. Parthasarathy, S.I. Rao, D.M. Dimiduk, M.D. Uchic, D.R. Trinkle, Contribution to size effect of yield strength from the stochastics of dislocation source lengths in finite samples, *Scripta Materialia* 56 (4) (2007) 313–316.
- [49] A. Joulain, L. Thilly, J. Rabier, Revisiting the defect structure of MAX phases: the case of Ti_4AlN_3 , *Philosophical Magazine* 88 (9) (2008) 1307–1320.
- [50] G.P. Bei, A. Guitton, A. Joulain, V. Brunet, S. Dubois, L. Thilly, C. Tromas, Pressure-enforced plasticity in MAX phases: from single grain to polycrystal investigation, *Philosophical Magazine* 93 (15) (2013) 1784–1801.
- [51] Y. Wada, N. Sekido, T. Ohmura, K. Yoshimi, Deformation microstructure developed by nanoindentation of a MAX phase Ti_2AlC , *Materials transactions* 59 (5) (2018) 771–778.
- [52] M.A. Tunes, R.W. Harrison, S.E. Donnelly, P.D. Edmondson, A Transmission Electron Microscopy study of the neutron-irradiation response of Ti-based MAX phases at high temperatures, *Acta Materialia* 169 (2019) 237–247.
- [53] Schmid, E. and Boas, W., 1950. Plasticity of crystals.
- [54] J.A. Barendreght, W.N. Sharpe Jr., The effect of biaxial loading on the critical resolved shear stress of zinc single crystals, *Journal of the Mechanics and Physics of Solids* 21 (2) (1973) 113–123.
- [55] I.P. Jones, W.B. Hutchinson, Stress-state dependence of slip in Titanium-6Al-4 V and other HCP metals, *Acta Metallurgica* 29 (6) (1981) 951–968.
- [56] W.A. Spitzig, Effect of hydrostatic pressure on plastic-flow properties of iron single crystals, *Acta Metallurgica* 27 (4) (1979) 523–534.
- [57] R.J. Asaro, Micromechanics of crystals and polycrystals, *Advances in applied mechanics* 23 (1983) 1–115.
- [58] K. Dang, D. Spearot, Pressure dependence of the Peierls stress in aluminum, *JOM* 70 (7) (2018) 1094–1099.
- [59] B. Escaig, Dissociation and mechanical properties. dislocation splitting and the plastic glide process in crystals, *Le Journal de Physique Colloques* 35 (C7) (1974) C7–151.
- [60] K. Dang, D. Bamney, L. Capolungo, D.E. Spearot, Mobility of dislocations in aluminum: The role of non-Schmid stress state, *Acta Materialia* 185 (2020) 420–432.
- [61] W. Cai, W.D. Nix, Imperfections in Crystalline Solids, Cambridge University Press, 2016.

- [62] R. Peierls, The size of a dislocation, *Proceedings of the Physical Society* 52 (1) (1940) 34–37.
- [63] W. Clegg, L. Vandeperre, J. Pitchford, Energy Changes and the Lattice Resistance, *Key Engineering Materials* 317-318 (2006) 271–276.
- [64] G. Plummer, M.W. Barsoum, C.R. Weinberger, G.J. Tucker, Basal dislocations in MAX phases: Core structure and mobility, *Materialia* 21 (2022), 101310.
- [65] S. Aryal, R. Sakidja, M.W. Barsoum, W.Y. Ching, A genomic approach to the stability, elastic, and electronic properties of the MAX phases, *physica status solidi (b)* 251 (8) (2014) 1480–1497.
- [66] J. Wang, Y. Zhou, Z. Lin, F. Meng, F. Li, Raman active phonon modes and heat capacities of Ti₂AlC and Cr₂AlC ceramics: first-principles and experimental investigations, *Applied Physics Letters* 86 (10) (2005), 101902.
- [67] F.D. León-Cázares, C.M.F. Rae, A stress orientation analysis framework for dislocation glide in face-centred cubic metals, *Crystals* 10 (6) (2020) 445.
- [68] A. Biguri, Perceptually Uniform Colormaps, MATLAB Central File Exchange, 2022.